ACS OMEGA

Open Access

http://pubs.acs.org/journal/acsodf

Article

Nonmetal Doping Modulates Fe Single-Atom Catalysts for Enhancement in Peroxidase Mimicking via Symmetry Disruption, Distortion, and Charge Transfer

Ling Liu, Xin Sun, Yonghui Li,* and Xiao-Dong Zhang*

Cite This: *ACS Omega* 2024, 9, 35144−35153

Read Online

ACCESS | Metrics & More | Article Recommendations | Supporting Information

ABSTRACT: Developing biomimetic catalysts with excellent peroxidase (POD)-like activity has been a long-standing goal for researchers. Doping nonmetallic atoms with different electronegativity to boost the POD-like activity of Fe−N−C single-atom catalysts (SACs) has been successfully realized. However, the introduction of heteroatoms to regulate the coordination environment of the central Fe atom and thus influence the activation of the H_2O_2 molecule in the POD-like reaction has not been extensively explored. Herein, the effect of different doping sites and numbers of heteroatoms (P, S, B, and N) on the adsorption and activation of H_2O_2 molecules of Fe−N sites is thoroughly investigated by density functional theory (DFT) calculations. In general, alternation in the catalytic efficiency directly depends on the transfer of electrons and the geometrical shifts near the Fe−N site. First, the symmetry disruption of the Fe−N_4 site by P, S, and B doping is beneficial to the activation of H_2O_2 due to a significant reduction in the adsorption energies. In some cases, without Fe−N_4 site disruption, the configurations fail to modulate the adsorption behavior of H_2O_2. Second, Fe−N−P/S configurations exhibit a stronger affinity for H_2O_2 molecules due to the significant out-of-plane distortions induced by larger atomic radii of P and S. Moreover, the synergistic effects of Fe and doping atoms P, S, and B with weaker electronegativity than that of N atoms promote electron donation to generated oxygen-containing intermediates, thus facilitating subsequent electron transfer with other substrates. This work demonstrates the critical role of tuning the coordinating environment of Fe−N active centers by heteroatom doping and provides theoretical guidance for controlling the types by breaking the symmetry of SACs to achieve optimal POD-like catalytic activity and selectivity.

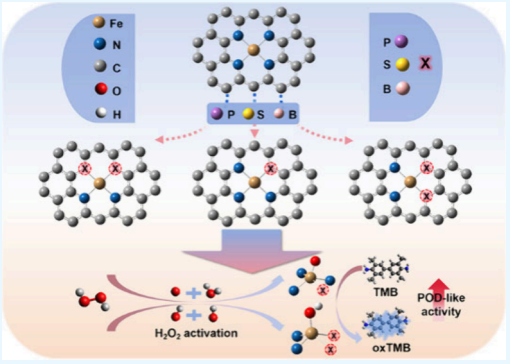

INTRODUCTION

Precisely designing and developing single-atom catalysts (SACs), which possess isolated active sites at the atomic level, have attracted considerable attention due to their maximum atom utilization, well-defined active sites, tunable coordination environments, and outstanding catalytic activity compared to that of conventional catalysts.[1−10] Fe−N−C SACs can effectively mimic the structure of the active center of natural peroxidase and exhibit exceptional peroxidase (POD)-like catalytic activity, thus realizing efficient H_2O_2 reduction, due to their precisely defined isolated iron active sites on the carbon substrate and possessing a structure similar to that of some natural enzymes.[11−15] In particular, Fe−N−C SACs have shown great potential in widespread applications, such as clinical medicine,[16] immunoassays,[17,18] and biosensing.[19,20] At the same time, many DFT-based methods have been successfully applied to predict the activities of nanomaterials acting as POD or catalase (CAT) mimics, particularly in relation to H_2O_2-targeted catalytic processes.[21−25] However, SACs with the standard symmetric planar four-coordination moieties (e.g., Fe−N_4) often show insufficient adsorption capability and catalytic activity for reactants due to their symmetrical charge distribution.[26] Thus, disrupting the symmetric electron pattern around the active sites may be crucial in tuning the adsorption of reaction intermediates on the catalysts, thereby boosting their catalytic activity.

Recent research has shown that two approaches for introducing atoms can effectively tune the electronic structure of M-N_x active centers and improve the catalytic activity. One approach is to introduce a second metal atom to form dual-metal active sites,[27,28] utilizing the d-band center coordination of the two metals to regulate the strength of adsorption of reaction intermediates such as Fe−Cu−N_x[29−31] and Fe_1Co_1−NC.[32] Another approach is to dope nonmetallic heteroatoms into the carbon substrate by replacing carbon atoms or altering the number of coordinating nitrogen atoms, thereby modifying the features of the symmetric charge distribution around the

Received: June 12, 2024
Revised: July 12, 2024
Accepted: July 19, 2024
Published: July 29, 2024

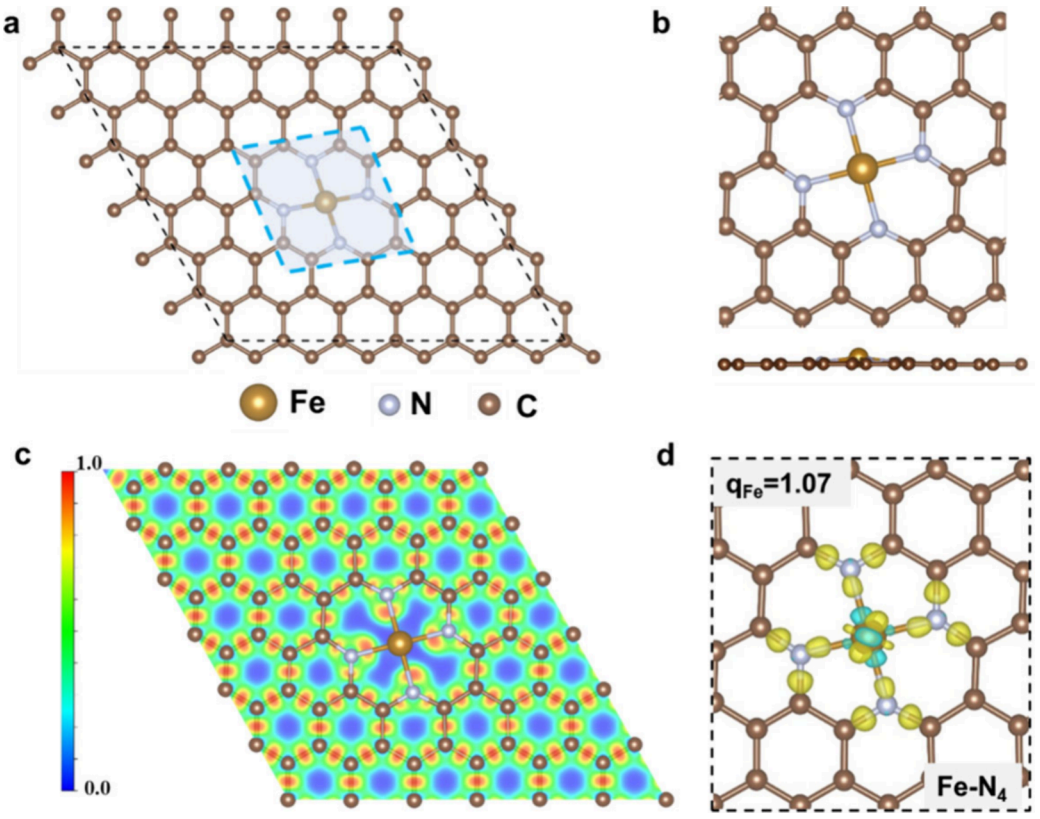

Figure 1. (a) Top view of the selected doping area in Fe−N_4. (b) Top and side views of the optimized geometries of FeN_4. (c) ELF image of Fe−N_4. (d) Charge density difference and Bader charge of FeN_4, where the blue (yellow) area represents charge density depletion (accumulation). The cutoff of the isosurface is 0.03 e $Bohr^{-3}$.

metal center. The synergistic effect generated by the charge transfer between the heteroatoms and central metal atoms plays a crucial role in catalytic activity. Many studies have demonstrated the effectiveness of the second approach,[33−35] especially doping heteroatoms into the carbon-based materials where M-N_4 sites embed in to enhance POD/CAT-like activity. Typical examples include Fe−N_4−B_2,[11] FeN_4C−SO_x,[36] Fe/CoNC−P,[14,37,38] and FeN_3−S.[39,40] Besides, based on previous reports, the coordination nitrogen environments of single atoms promote differences in catalytic activity. Fe_{Fer}−SAC with four coordinating N atoms has highest POD-like catalytic activity among the three Fe SACs due to the lower OH generation barrier.[41] And the FeN_5 with axial N coordination exhibits superior POD/OXD (oxidase)-like activity owing to a clear electron push effect.[26,42] In a word, the atomic radius, electronegativity, doping ratio, and doping position of different heteroatoms are crucial factors influencing catalytic activity and selectivity.[43,44] However, most theoretical studies focus on only one or two of these aspects and most analyses are based on experimental results, while a comprehensive and in-depth study of doping factors for the binding affinity of H_2O_2 linked to POD-like activity at the theoretical level is lacking.

In this work, the modulation of H_2O_2 molecule adsorption behavior by heteroatoms (P, S, B, and N) in Fe−N structures at different doping positions and numbers is systematically investigated. DFT calculations suggest that the synergistic effects between the Fe site and heteroatoms in Fe−N configurations, particularly those disrupting the symmetry of the Fe−N_4 geometry, optimize the adsorption behavior and activation of H_2O_2, thus facilitating electron transfer between the catalysts and generated oxygen-containing intermediates. In addition, the incorporation of P and S atoms with larger atomic radii in the Fe−N configurations induces significant surface distortion, enhancing the affinity for H_2O_2 molecules. Moreover, the synergistic effects of Fe and doping atoms P, S, and B with weaker electronegativity than that of N promote the activation of H_2O_2 and the formation of oxygen-containing intermediates, facilitating subsequent electron transfer with other substrates, such as 3,3′,5,5′-tetramethylbenzidine (TMB). Replacing C atoms around the intact Fe−N_4 structure by N fails to modulate H_2O_2 adsorption behavior. Therefore, asymmetric atomic Fe−N configurations achieve optimal geometric and electronic structure and play a crucial role in promoting H_2O_2 adsorption and activation for POD-like reaction kinetics.

COMPUTATIONAL MODELS AND METHODS

To explore the geometric and electronic structure of heteroatom (P, S, B, and N) doping Fe−N configurations, a 6 × 6 × 1 N-doped carbon layer with an Fe atom anchored on the N_4 vacancy is built to model the Fe−N_4−C structure (Figure 1a). According to previous studies,[11,14,38−40,43−50] both coordinating N and neighboring C atoms around the central Fe are the sites that can be doped, and the blue area inside the dashed box in Figure 1a is chosen as the doping region for heteroatoms. To eliminate the interaction between atoms in adjacent periodic layers, a vacuum layer of up to 15 Å is added to the surface of the N-doped carbon layer along the z direction.

All spin polarization calculations are based on DFT using the Vienna ab initio simulation package (VASP).[51,52] To describe

https://doi.org/10.1021/acsomega.4c04990
ACS Omega 2024, 9, 35144−35153

the electron−ion interaction, the projector augmented wave (PAW)[53,54] method is employed. The electron exchange and correlation energies are treated within the generalized gradient approximation in the Perdew−Burke−Ernzerhof formalism (GGA-PBE).[55] The van der Waals (vdW) interaction is considered by using the DFT-D3[56,57] method of Grimme. In structural relaxations, the convergence criteria for energies and forces are set to 1×10^{-6} eV and 0.01 eV/Å, respectively, and *k*-point meshes of 3 × 3 × 1 are used for the models.[58] The convergence of calculations is ensured by setting the cutoff energy for the plane-wave basis at 500 eV. A simple rotationally invariant DFT+U[59] version is adopted to address the electronic correlation of Fe 3d electrons, where a value of U = 3.0 eV is used for Fe atoms. Crystal orbital Hamilton population (COHP) analysis is performed by utilizing the Lobster program.[60,61]

The formation energy (E_{form}) of heteroatom-doped Fe−N configurations can be achieved by taking undoped Fe−N_4 as a reference

$$E_{form} = E_{Fe-N-X} + m\mu_{N/C} - E_{Fe-N_4} - m\mu_X \quad (1)$$

where E_{Fe-N_4} and E_{Fe-N-X} represent the total energies of FeN_4 and heteroatom X (X = P, S, B, and N)-doped Fe−N configurations, respectively. μ_N, μ_C, and μ_X represent the chemical potentials of N, C, and X, respectively. Here, the E_{form} of heteroatom-doped Fe−N configurations can be obtained by taking undoped Fe−N_4 as a reference, and the lower formation energies indicate a more stable structure after doping. The adsorption energies of H_2O_2 ($\Delta E_{H_2O_2}$) are calculated according to

$$\Delta E_{H_2O_2} = E_{H_2O_2^*} - E_{H_2O_2} - E_{sur} \quad (2)$$

where $E_{H_2O_2*}$ represents the total energy of the H_2O_2 adsorption state, $E_{H_2O_2}$ represents the energy of H_2O_2 molecules, and E_{sur} represents the total energy of the clean surface of the Fe−N structure. The adsorption energy of H_2O_2 on some Fe−N structures is calculated by assessing the reaction energy where the H_2O_2 molecule in gas undergoes heterolysis (O* + H_2O*) or homolysis (OH* + OH*). The reaction energy (ΔE_r) is calculated by

$$\Delta E_r = E_{FS} - E_{IS} \quad (3)$$

where E_{FS} and E_{IS} are the total energies of the corresponding final state (FS) and initial state (IS), respectively.

Figure 1b shows the top and side views of the optimized geometry of the Fe−N_4 configuration, and it shows that all atoms in the Fe−N_4 structure are kept nearly in the same plane. With the incorporation of the Fe atom, unpaired electrons as well as lone-pair electrons of N atoms contribute to Fe−N interactions, which are displayed in the electron localization function (ELF) image in Figure 1c. Additionally, the charge density difference in Figure 1d indicates that the charge distribution of the Fe−N_4 configuration is symmetrical, indicating symmetric Fe−N coordination. For Fe−N_4, the central Fe atom loses electrons while the coordinating N atoms gain electrons. Moreover, the calculated Bader charge of Fe is 1.07, further confirming that Fe donates electrons, making its charge positive. The undoped Fe−N_4 structure serves as a benchmark.

RESULTS AND DISCUSSION

Stability of Heteroatom-Doped Fe−N Configurations. As shown in Figures S1−S4, the E_{form} values of all proposed heteroatom-doped Fe−N structures, including Fe−N_3X_1 and isomers of Fe−N_4X_1, Fe−N_4X_2, and Fe−N_2X_2 (X= P, S, B, and N), are listed. In addition to Fe−N_3X_1, the two structures with the lowest formation energies (blue-labeled configurations in Figures S1−S4) according to eq 1 are first selected from each type of isomer for geometry and charge distribution studies. Besides, 15 configurations with relatively lower E_{form} and thus better stability are further selected, including the undoped Fe−N_4 and heteroatom-doped Fe−N configurations (marked with red asterisks in Figures 2−4h and 5e), to investigate the effects of dopant atoms on the adsorption behavior of H_2O_2 related to POD-like activity.

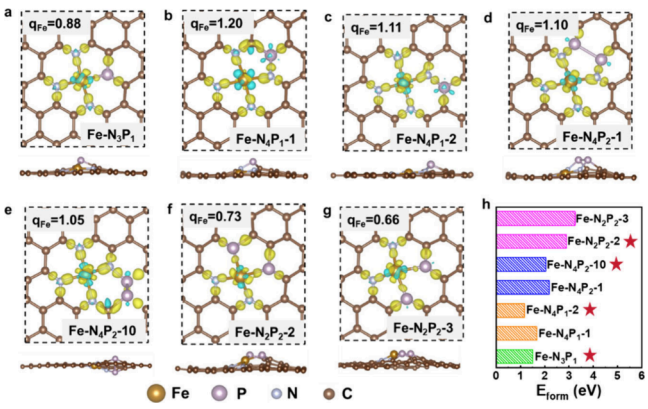

Figure 2. (a−g) Charge density differences, Bader charge, and side view of optimized geometries of Fe−N_3P_1, Fe−N_4P_1-1, Fe−N_4P_1-2, Fe−N_4P_2-1, Fe−N_4P_2-10, Fe−N_2P_2-2, and Fe−N_2P_2-3 configurations, respectively, where the blue (yellow) area represents charge density depletion (accumulation). The cutoff of the isosurface is 0.03 e $Bohr^{-3}$. (h) Formation energies of doping with different sites and numbers (1, 2) of P atoms in Fe−N_4.

The results show that B- and N-doped Fe−N configurations are relatively more stable due to the lower E_{form}, while the P and S doping both slightly lower the stability of the entire Fe−N configurations. As shown in Figures 2−4h and 5e, for P, S, and N doping, the overall trend in E_{form} increases with the increase in the number of dopant atoms, indicating that the stability of the structure decreases. Besides, replacing the coordinated N atoms with P, S, and B greatly reduces the stability compared to replacing C atoms, when the number of doped atoms reaches 2. It is noteworthy that substituting C atoms adjacent to the active site with B atoms is energetically more favorable due to E_{form} being negative.

Doping-Induced Geometrical Change. By benchmarking with the original geometry of the Fe−N_4 site, the doped P and S atoms shift the geometry significantly, while the B or N atoms do not change the planar shape in the geometry. As shown in Figures 2 and 3, the introduction of heteroatoms P and S induces out-of-plane distortions due to the longer P/S−C bond (1.75−1.78 Å) compared to N−C (1.36−1.38 Å) in the structure. The more P/S atoms doped into the Fe−N SAC, the more buckling of planar configurations exhibited, and the changes in Fe−N distances are shown in Table S1. The apparent lengthening or shortening of the Fe−N distances in the Fe−N−P/S configurations in Table S1, compared to the Fe−N distance (1.97−1.98 Å) in Fe−N_4, also demonstrates

https://doi.org/10.1021/acsomega.4c04990
ACS Omega 2024, 9, 35144−35153

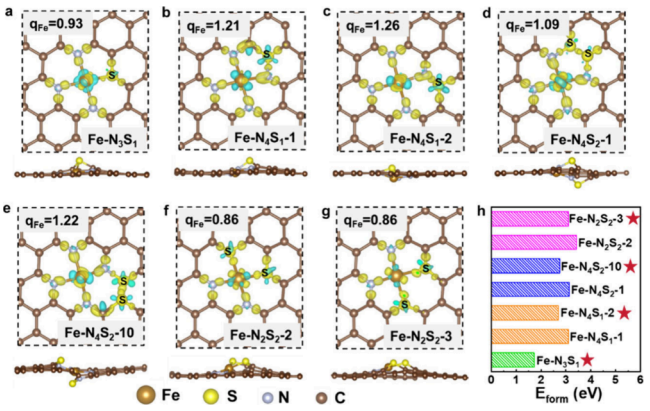

Figure 3. (a–g) Charge density differences, Bader charge, and side view of optimized geometries of Fe–N_3S_1, Fe–N_4S_1-1, Fe–N_4S_1-2, Fe–N_4S_2-1, Fe–N_4S_2-10, Fe–N_2S_2-2, and Fe–N_2S_2-3 configurations, respectively, where the blue (yellow) area represents charge density depletion (accumulation). The cutoff of the isosurface is 0.03 e $Bohr^{-3}$. (h) The formation energies of doping with different sites and numbers (1, 2) of S atoms in Fe–N_4.

the distortions. This can be rationalized by the fact that the atomic radii of P and S are larger than those of B, C, and N.

Doping-Induced Electronic Structure Change. The local electronic structure shifts of Fe are analyzed by the charge density difference. As shown in the charge distribution in Figures 2–4, the replacement of coordinating N by

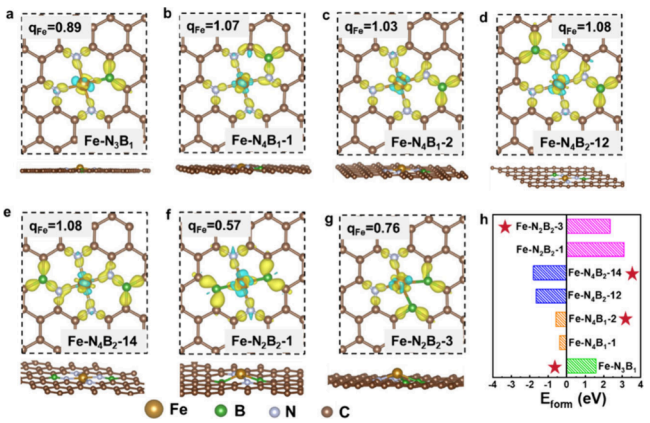

Figure 4. (a–g) Charge density differences, Bader charge, and side view of optimized geometries of Fe–N_3B_1, Fe–N_4B_1-1, Fe–N_4B_1-2, Fe–N_4B_2-12, Fe–N_4B_2-14, Fe–N_2B_2-1, and Fe–N_2B_2-3 configurations, respectively, where the blue (yellow) area represents charge density depletion (accumulation). The cutoff of the isosurface is 0.03 e $Bohr^{-3}$. (h) Formation energies of doping with different sites and numbers (1, 2) of B atoms in Fe–N_4.

heteroatoms leads to a marked decrease in the positive charge of the central Fe, as confirmed by the reduced Bader charge of Fe–N_3X_1 (Figures 2–4a) and a further reduction in Fe–N_2X_2 (X = P, S, B) (Figures 2–4f,g). This decrease is attributed to the weaker electronegativity of P/S/B than N atoms, allowing P/S/B → Fe → N electron transfer.[14,62] Due to the electron donation of P, S, and B, the depletion of charge on the central Fe atom is weakened, resulting in a reduction in the positive charge of Fe.

On the other hand, the substitution of C atoms around the Fe–N_4 site by heteroatoms is taken into account. First, for P and S doping, the dopant atoms lose electrons to the neighboring C and N atoms, and the central Fe atom loses more electrons, especially for S doping, leading to an increase in its positive charge (Figures 2b–d and 3b–e). For B doping, the change in the positive charge of Fe is not significant compared to the undoped state of 1.07 (Figure 4b–e). Finally, when additional N atoms are doped into the C substrate around the Fe–N_4 site, replacing one C atom cannot induce significant shifts in the charge transfer of Fe (Figure 5a,b). However, as the number of substitutions increases, the electron donation from Fe decreases, which is confirmed by the less positive charge of Fe (Figure 5c,d).

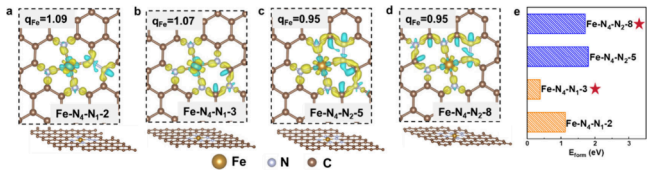

Figure 5. (a–d) Charge density differences, Bader charge, and side view of optimized geometries of Fe–N_4-N_1-2, Fe–N_4-N_1-3, Fe–N_4-N_2-5, and Fe–N_4-N_2-8 configurations, respectively, where the blue (yellow) area represents charge density depletion (accumulation). The cutoff of the isosurface is 0.03 e $Bohr^{-3}$. (e) Formation energies of doping with different sites and numbers (1, 2) of N atoms in Fe–N_4.

Work Functions and DOS Analysis. To assess the capacity of electron transfer, work functions and the projection density of states (PDOS) are investigated. As indicated in the configurations summarized in Table 1, the work functions of the P- and B-doped Fe–N structures are overall improved over the undoped Fe–N_4 while doping with S and N leads to a decrease in work functions. Especially for N-doped Fe–N_4 structures, increasing the proportion of N doping on the carbon substrate triggers a significant decrease in the work function (~3.600 eV). This is attributed to the higher electronegativity of N atoms, which attracts more electrons to the catalyst surface, leading to a decrease in the work function. The lower work function of the catalyst indicates the higher capacity of electron donation and the fact that electron transfer can be facilitated.[63–65]

In addition, the PDOSs of Fe active sites in Figure 6 exhibit prominent electronic states near the Fermi level, with narrow band gaps in the configurations doped with P, S, B, and N. In contrast, there is a considerable band gap in the associated PDOS in the undoped Fe–N_4. Therefore, the addition of new heteroatoms (P, S, B, and N) can substantially alter the PDOSs of the active sites, which may result in decreasing the energy barrier for species' adsorption in catalytic reactions.[66,67]

Doping Effects on Adsorption and Activation of H_2O_2 in the POD-like Reaction. To further explore the modulation of H_2O_2 adsorption and activation on Fe–N configurations by heteroatom doping, adsorption geometries and $\Delta E_{H_2O_2}$ are analyzed (Figure 7). Based on computational results, the weaker electronegativity and larger atomic radius of doping atoms compared to those of N atoms and the disruption of the symmetrical Fe–N_4 site appear to be effective in promoting the adsorption and activation of H_2O_2. First, substituting coordinating N atoms with heteroatoms to disrupt the Fe–N_4 site is favorable for H_2O_2 activation, such as Fe–N_3X_1 (Figure 7a,e,i) and Fe–N_2X_2 (X = P, S, and B) configurations (Figure 7d,h,l). As expected, these structures

https://doi.org/10.1021/acsomega.4c04990
ACS Omega 2024, 9, 35144–35153

Table 1. Calculated Work Functions (eV) of the Heteroatom (P, S, B, and N)-Doped Fe−N Configurations

Structure		Work function	Structure		Work function
	$Fe-N_4$	4.216			
P-doped	$Fe-N_3P_1$	4.303	B-doped	$Fe-N_3B_1$	4.211
	$Fe-N_4P_1$-2	4.228		$Fe-N_4B_1$-2	4.323
	$Fe-N_4P_2$-10	4.196		$Fe-N_4B_2$-14	4.377
	$Fe-N_2P_2$-2	4.333		$Fe-N_2B_2$-3	4.299
S-doped	$Fe-N_3S_1$	3.909	N-doped	$Fe-N_4-N_1$-3	3.526
	$Fe-N_4S_1$-2	4.063			
	$Fe-N_4S_2$-10	4.066		$Fe-N_4-N_2$-8	3.600
	$Fe-N_2S_2$-3	4.121			

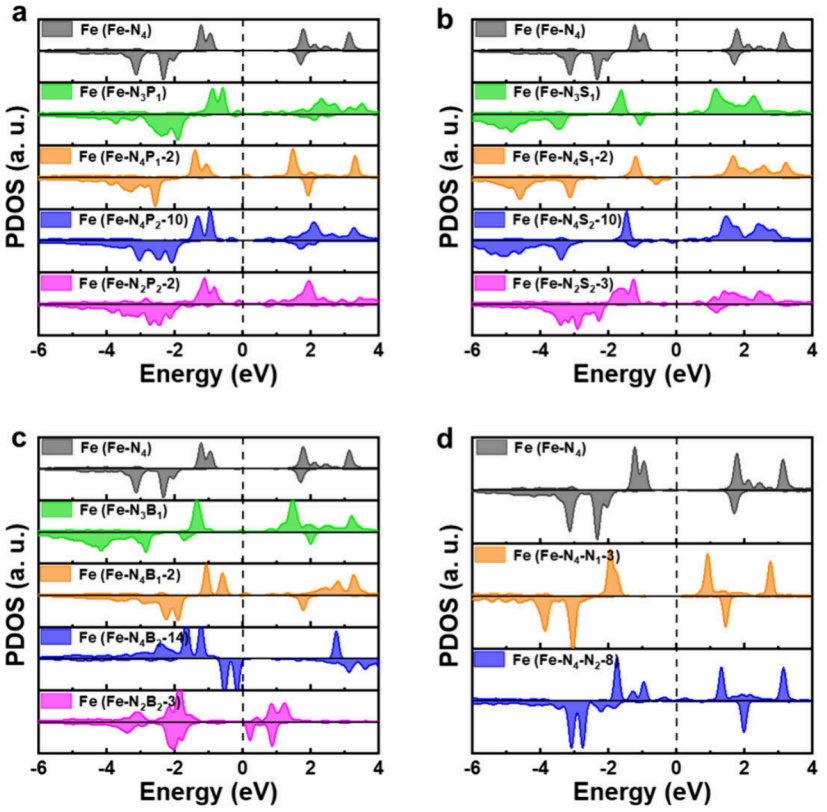

Figure 6. Projected electronic density of state (PDOS) of Fe in (a) P-doped, (b) S-doped, and (c) B-doped Fe−N and (d) N-doped $Fe-N_4$ configurations. The undoped $Fe-N_4$ serves as a reference.

exhibit lower adsorption energies for H_2O_2 in comparison to undoped $Fe-N_4$ (−0.318 eV), potentially enhancing the adsorption and reaction kinetics of H_2O_2. Specifically, H_2O_2 molecules are readily activated and undergo heterolysis (O* + H_2O*) on $Fe-N_3P_1$, $Fe-N_2P_2$-2, $Fe-N_3S_1$, and $Fe-N_3B_1$, and the generated O readily attaches to the central Fe with Fe−O distances of 1.66, 1.67, 1.68, and 1.87 Å, respectively (Figure 7a,d,e,i). Besides, $Fe-N_2S_2$-3 and $Fe-N_2B_2$-3 tend to induce homolysis (OH*+OH*), as shown in Figure 7h,l, where one of the generated OHs attaches to the central Fe with Fe−O distances of 1.85 and 1.84 Å, respectively. These shorter Fe−O distances compared to 2.32 Å on $Fe-N_4$ (the reference in Figure 7m) indicate the stronger adsorption and beneficial activation of H_2O_2 molecules.

In addition, configurations in which neighboring C atoms are replaced without breaking the N_4 structure fail to optimize the adsorption behavior of H_2O_2. Similar to the undoped $Fe-N_4$, whole H_2O_2 molecules adsorb on active sites of $Fe-N_4X_1$ (Figure 7f,j,n) and $Fe-N_4X_2$ (X = S, B, and N) (Figure 7g,k,o) with Fe−O distances of 2.27−2.48 Å, most of which are longer than the Fe−O distance on $Fe-N_4$. Besides, adsorption energies for H_2O_2 are not significantly lower compared with FeN_4 (−0.318 eV). These results indicate that relatively weak adsorptions of H_2O_2 are therefore unfavorable for subsequent activation. For $Fe-N_4P_1$-2 and FeN_4P_2-10 (Figure 7b,c), although H_2O_2 molecules also experience heterolysis on active sites, the formed O* is adsorbed on P atoms instead of the central Fe. Due to the quite low adsorption energies (−4.949 and −4.334 eV, respectively), the interaction between the O* species and P is too strong to facilitate subsequent electron extraction from other substrates in the POD-like catalytic reaction.

PDOS and COHP Analysis. The PDOS and the projected crystal orbital Hamilton population (-pCOHP) analysis of Fe−O are carried out to further examine the influence by the heteroatom doping on the interaction between Fe sites and H_2O_2 or oxygen species-related intermediates (O*, OH*, and H_2O*) after adsorption. Simulation results suggest that the

https://doi.org/10.1021/acsomega.4c04990
ACS Omega 2024, 9, 35144−35153

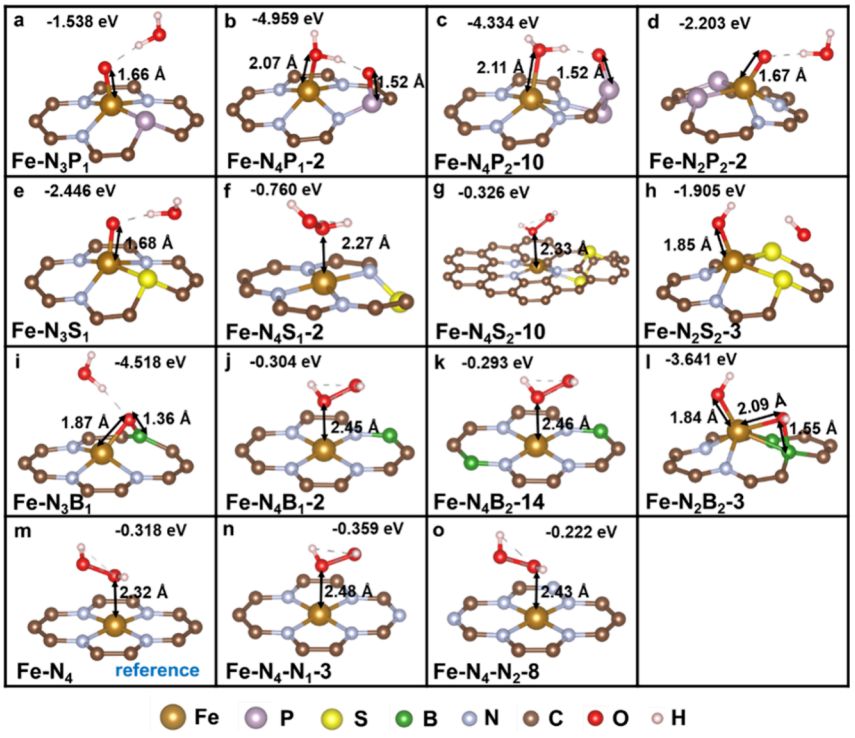

Figure 7. Optimized geometries, $\Delta''E_{H_2O_2}$, and corresponding Fe−O and X−O distances of H_2O_2 adsorption on heteroatom (X = P, S, B, and N)-doped Fe−N configurations. The undoped Fe−N_4 serves as a reference.

heteroatom (P, S, and B) doping Fe−N configurations with the symmetry disruption of N_4 geometry have a stronger affinity for H_2O_2 molecules, which would be beneficial for their activation, thus accelerating the reaction kinetics. In the simulation, the d-band center of Fe and the p-band center of O* in Fe−O for each adsorption configuration are also provided. Since most reaction intermediates are related to oxygen species, the adsorption of O is taken as an example.[68]

As shown in the left panel of Figure 8a,d,e,h,i,l, the symmetry breaking of N_4 induced by P/S/B doping narrows the gap between the d-band center and the p-band center. Consequently, this increases the overlap of Fe 3d with O 2p orbitals in comparison to Fe−N_4 (Figure 8m), indicating the enhanced interactions between the central Fe in Fe−N_3X_1 and Fe−N_2X_2 (X = P, S, and B) and oxygen species-related intermediates. This effective activation of H_2O_2 is further confirmed quantitatively by the integrated pCOHP to the Fermi level (ICOHP) for the Fe−O interaction quantitatively.

As shown in the COHP diagram in Figure 8a,d,e,h,i,l, the calculated ICOHPs of Fe−O on Fe−N_3X_1 and Fe−N_2X_2 (X = P, S, and B) configurations are more negative than that on Fe−N_4 (−0.63 eV), which indicates a greater number of electrons occupying bonding orbitals, leading to the stronger Fe−O interaction. Therefore, substituting coordinating N atoms with the P, S, and B promotes the adsorption and then activation of the H_2O_2, resulting in stronger bonding between Fe and the adsorbed oxygen-containing intermediates, consequently expediting the reaction kinetics.

However, for Fe−N_4X_1 (Figure 8f,j,n) and Fe−N_4X_2 (X = S, B, and N) (Figure 8g,k,o) configurations, there is no substantial decrease in the energy difference between the d-band center of Fe and the p-band center of O*, and ICOHP values for Fe−O* are relatively close to that of Fe−N_4 (−0.63 eV), indicating similar interaction strengths. For Fe−N_4P_1-2 and FeN_4P_2-10 (Figure 8b,c), the weak interaction between the Fe and O* (in H_2O) is also confirmed by the small overlap of Fe 3d with O 2p orbitals due to the antibonding greatly lowered below the Fermi level compared to Fe−N_3X_1 and Fe−N_2X_2 structures, suggesting that produced H_2O molecules show relatively weak adsorption strength. The stronger interaction between the generated O* and P will be discussed later.

Electron Transfer and Charge Redistribution after Adsorption and Activation of H_2O_2. To further assess the electron transfer ability quantitatively, the charge redistribution between H_2O_2 or oxygen-containing intermediates and the 15 Fe−N configurations in Table 1 is investigated. The calculations reveal that the electronic synergistic effect triggered by N_4 symmetry disruption in Fe−N_3X_1 and Fe−N_2X_2 (X = P, S, and B) configurations is beneficial to the H_2O_2 activation and the subsequent electron transfer from other substrates, such as TMB.

As exhibited by the charge density differences and Bader charge in Figure 9, Fe sites and dopant atoms (P, S, and B) consistently act as electron donors, while the generated OH* and O* are electron acceptors. Specifically, in the case of replacing coordinating N atoms, the central Fe is also the intermediate of charge transfer, and the electrons lost by the dopant atom P/S/B are transferred to O* and OH* via Fe sites (synergistic effects of Fe and P/S/B atoms) in Fe−N_3X_1 and Fe−N_2X_2 configurations, which is confirmed by the calculated Bader charges of Fe before (Figures 2−5) and after adsorption, O* and OH* (Figure 9a,d,e,h,i,l).

The weak adsorption strength between the formed H_2O and active sites is also evidenced by the Bader charge of the H_2O (close to 0), indicating that the regeneration of catalytic active sites would occur rapidly after the generation of H_2O molecules and may lower the dehydration energy barrier of

https://doi.org/10.1021/acsomega.4c04990
ACS Omega 2024, 9, 35144−35153

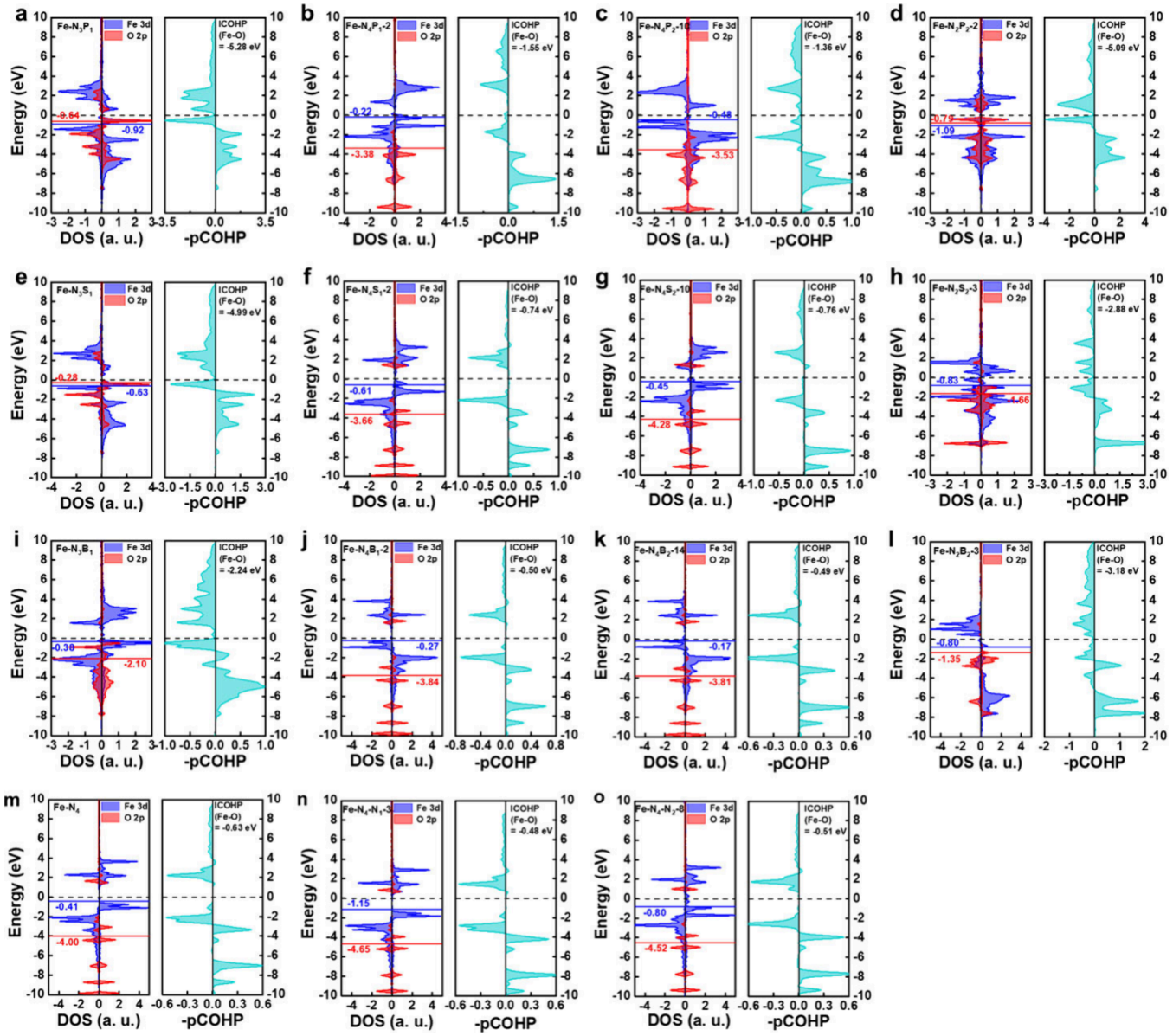

Figure 8. PDOS and pCOHP of the oxygen adsorption state of H_2O_2 for (a–d) P-doped, (e–h) S-doped, and (i–l) B-doped Fe–N and (m–o) undoped and N-doped Fe–N_4 configurations. The PDOS and pCOHP of the oxygen adsorption state in undoped FeN_4 serve as a reference.

the H_2O_2 molecule. Moreover, since the numbers of electrons obtained by the O* in Fe–N_3P_1 and Fe–N_3S_1 (−0.75 and −0.85, respectively) are less than that of Fe–N_3B_1 (−1.33), this would better stimulate the O* to extract electrons from substrates, such as TMB, in the POD-like reaction for Fe–N_3P_1 and Fe–N_3S_1.

Meanwhile, as confirmed by the calculated Bader charges of H_2O_2 molecules (close to 0) adsorbed on Fe–N_4X_1 (Figure 9f,j,n) and Fe–N_4X_2 (X = S, B, and N) (Figure 9g,k,o), the Fe site exhibits a weak interaction with the H_2O_2, thereby failing to activate the H_2O_2. Although the H_2O_2 is activated on the Fe–N_4P_1 and Fe–N_4P_2-2, the stronger interaction is confirmed by the Bader charge of the O* adsorbed on the P atom (−1.40 in Figure 9b,c), which is significantly more than the electrons gained by adsorption on the Fe sites of Fe–N_3P_1 (−0.75), Fe–N_3S_1 (−0.85), and Fe–N_2P_2-1 (−0.79). This is not conducive to facilitating subsequent electron extraction from other substrates, such as Fe–N_4P_1 and Fe–N_4P_2-2. Therefore, doping P, S, and B atoms with weaker electronegativity than N in N_4-symmetry-breaking Fe–N configurations achieves the optimal electron density distribution of the active site. However, without Fe–N_4 site disruption, the Fe–N_4X_1 and Fe–N_4X_2 configurations fail to modulate the adsorption behavior of H_2O_2 and effectively facilitate electron transfer with the adsorbates.

■ CONCLUSIONS

In this work, the influence of heteroatom (P, S, B, and N) doping on the adsorption and activation of H_2O_2 molecules by modulating the microenvironment of Fe–N–X (X= P, S, B, and N) sites, which is crucial to enhancing POD-like activity, is investigated based on DFT calculations. The results reveal that the synergistic effects of the central Fe and heteroatoms in Fe–N configurations with a symmetry disruption of Fe–N_4 geometry optimize the adsorption of H_2O_2, thus facilitating H_2O_2 activation and the subsequent electron transfer between

https://doi.org/10.1021/acsomega.4c04990
ACS Omega 2024, 9, 35144−35153

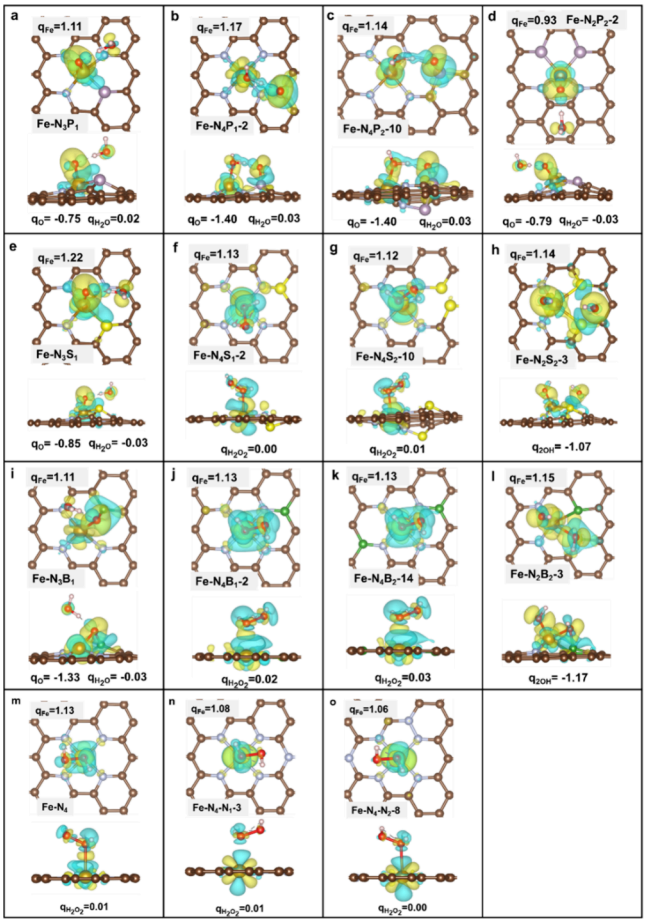

Figure 9. Charge density differences (the isosurface level is 0.004 e Bohr^{-3}) of H_2O_2 adsorbed on (a−d) P-doped, (e−h) S-doped, (i−l) B-doped Fe−N, and (m−o) undoped and N-doped Fe−N_4 configurations (the yellow and blue represent gaining and losing electrons, respectively). The Bader charge of Fe and adsorbates is also shown in the figure.

catalysts and generated oxygen-containing intermediates. Additionally, the introduction of P and S atoms with larger atomic radii in the Fe−N configurations induces significant out-of-plane distortions, enhancing the affinity for H_2O_2 molecules. Moreover, the synergistic effects of Fe and doping atoms P, S, and B with weaker electronegativity than N promote the activation of H_2O_2 and the generation of oxygen-containing intermediates, facilitating subsequent electron transfer with other substrates. Introducing N around the intact Fe−N_4 structure fails to tune the H_2O_2 adsorption behavior; therefore, symmetry disruption of the Fe−N_4 site plays a crucial role in promoting H_2O_2 adsorption and activation for Fe−N configurations linked to POD-like catalytic reactions.

This study is limited by the type of doping elements. Further exploration of the other types of doping heteroatoms, doping distance, and doping proportion of heteroatoms should be addressed. This study demonstrates the critical role of tuning the coordinating environment of Fe−N active centers by heteroatom doping and provides theoretical guidance for controlling the types by means of breaking the symmetry of SACs to achieve optimal POD-like catalytic activity and selectivity.

■ ASSOCIATED CONTENT

Supporting Information

The Supporting Information is available free of charge at https://pubs.acs.org/doi/10.1021/acsomega.4c04990.

All simulated geometries and corresponding formation energies of P-, S-, B-, and N-doped Fe−N configurations (PDF)

■ AUTHOR INFORMATION

Corresponding Authors

Yonghui Li − *Department of Physics and Tianjin Key Laboratory of Low Dimensional Materials Physics and Preparing Technology, School of Sciences, Tianjin University, Tianjin 300350, China*; Email: yonghui.li@tju.edu.cn

Xiao-Dong Zhang − *Tianjin Key Laboratory of Brain Science and Neural Engineering, Academy of Medical Engineering and Translational Medicine, Tianjin University, Tianjin 300072, China; Department of Physics and Tianjin Key Laboratory of Low Dimensional Materials Physics and Preparing Technology, School of Sciences, Tianjin University, Tianjin 300350, China*; orcid.org/0000-0002-7212-0138; Email: xiaodongzhang@tju.edu.cn

Authors

Ling Liu − *Tianjin Key Laboratory of Brain Science and Neural Engineering, Academy of Medical Engineering and Translational Medicine, Tianjin University, Tianjin 300072, China*

Xin Sun − *Tianjin Key Laboratory of Brain Science and Neural Engineering, Academy of Medical Engineering and Translational Medicine, Tianjin University, Tianjin 300072, China*

Complete contact information is available at: https://pubs.acs.org/10.1021/acsomega.4c04990

Author Contributions

All authors have discussed the results and contributed to the manuscript.

Notes

The authors declare no competing financial interest.

■ ACKNOWLEDGMENTS

This work was financially supported by the National Key Research and Development Program of China (nos. 2021YFF1200700 and 2021YFF1200701), the National Natural Science Foundation of China (nos. 91859101, 81971744, U1932107, 82001952, 11804248, 82302361, and 82302381), Outstanding Youth Funds of Tianjin (no. 2021FJ-0009), STI 2030-Major Projects (no. 2022ZD0210200), the National Natural Science Foundation of Tianjin (nos. 19JCZDJC34000, 20JCYBJC00940, 21JCYBJC00550, 21JCZDJC00620, and 21JCYBJC00490), the Key Projects of Tianjin Natural Fund (no. 21JCZDJC00490), the Innovation Foundation of Tianjin University, the China Postdoctoral Science Foundation (no. 2023M732601), and the CAS Interdisciplinary Innovation Team (no. JCTD-2020-08).

■ REFERENCES

(1) Gao, L.; Zhuang, J.; Nie, L.; Zhang, J.; Zhang, Y.; Gu, N.; Wang, T.; Feng, J.; Yang, D.; Perrett, S.; Yan, X. Intrinsic Peroxidase-like Activity of Ferromagnetic Nanoparticles. *Nat. Nanotechnol.* **2007**, *2* (9), 577−583.

(2) Qiao, B.; Wang, A.; Yang, X.; Allard, L. F.; Jiang, Z.; Cui, Y.; Liu, J.; Li, J.; Zhang, T. Single-Atom Catalysis of CO Oxidation Using Pt_1/FeO_x. *Nat. Chem.* **2011**, *3* (8), 634−641.
(3) Chen, Y.; Ji, S.; Chen, C.; Peng, Q.; Wang, D.; Li, Y. Single-Atom Catalysts: Synthetic Strategies and Electrochemical Applications. *Joule* **2018**, *2* (7), 1242−1264.
(4) Zhu, C.; Fu, S.; Shi, Q.; Du, D.; Lin, Y. Single-Atom Electrocatalysts. *Angew. Chem., Int. Ed.* **2017**, *56* (45), 13944−13960.
(5) Ji, S.; Chen, Y.; Wang, X.; Zhang, Z.; Wang, D.; Li, Y. Chemical Synthesis of Single Atomic Site Catalysts. *Chem. Rev.* **2020**, *120* (21), 11900−11955.
(6) Gao, C.; Low, J.; Long, R.; Kong, T.; Zhu, J.; Xiong, Y. Heterogeneous Single-Atom Photocatalysts: Fundamentals and Applications. *Chem. Rev.* **2020**, *120* (21), 12175−12216.
(7) Wu, W.; Huang, L.; Wang, E.; Dong, S. Atomic Engineering of Single-Atom Nanozymes for Enzyme-like Catalysis. *Chem. Sci.* **2020**, *11* (36), 9741−9756.
(8) Wu, D.; Li, J.; Xu, S.; Xie, Q.; Pan, Y.; Liu, X.; Ma, R.; Zheng, H.; Gao, M.; Wang, W.; Li, J.; Cai, X.; Jaouen, F.; Li, R. Engineering Fe-N Doped Graphene to Mimic Biological Functions of NADPH Oxidase in Cells. *J. Am. Chem. Soc.* **2020**, *142* (46), 19602−19610.
(9) Xie, X.; He, C.; Li, B.; He, Y.; Cullen, D. A.; Wegener, E. C.; Kropf, A. J.; Martinez, U.; Cheng, Y.; Engelhard, M. H.; Bowden, M. E.; Song, M.; Lemmon, T.; Li, X. S.; Nie, Z.; Liu, J.; Myers, D. J.; Zelenay, P.; Wang, G.; Wu, G.; Ramani, V.; Shao, Y. Performance Enhancement and Degradation Mechanism Identification of a Single-Atom Co-N-C Catalyst for Proton Exchange Membrane Fuel Cells. *Nat. Catal.* **2020**, *3* (12), 1044−1054.
(10) Li, P.; Gao, X. J.; Gao, X. Theoretical Investigation on the Oxidoreductase-Mimicking Activity of Carbon-Based Nanozyme. In *ACS Symposium Series*; Wang, X., Ed.; American Chemical Society: Washington, DC, 2022; Vol. *1422*, pp 67−89.
(11) Jiao, L.; Xu, W.; Zhang, Y.; Wu, Y.; Gu, W.; Ge, X.; Chen, B.; Zhu, C.; Guo, S. Boron-Doped Fe-N-C Single-Atom Nanozymes Specifically Boost Peroxidase-like Activity. *Nano Today* **2020**, *35*, 100971.
(12) Jiao, L.; Wu, J.; Zhong, H.; Zhang, Y.; Xu, W.; Wu, Y.; Chen, Y.; Yan, H.; Zhang, Q.; Gu, W.; Gu, L.; Beckman, S. P.; Huang, L.; Zhu, C. Densely Isolated FeN_4 Sites for Peroxidase Mimicking. *ACS Catal.* **2020**, *10* (11), 6422−6429.
(13) Jiao, L.; Xu, W.; Yan, H.; Wu, Y.; Liu, C.; Du, D.; Lin, Y.; Zhu, C. Fe-N-C Single-Atom Nanozymes for the Intracellular Hydrogen Peroxide Detection. *Anal. Chem.* **2019**, *91* (18), 11994−11999.
(14) Ji, S.; Jiang, B.; Hao, H.; Chen, Y.; Dong, J.; Mao, Y.; Zhang, Z.; Gao, R.; Chen, W.; Zhang, R.; Liang, Q.; Li, H.; Liu, S.; Wang, Y.; Zhang, Q.; Gu, L.; Duan, D.; Liang, M.; Wang, D.; Yan, X.; Li, Y. Matching the Kinetics of Natural Enzymes with a Single-Atom Iron Nanozyme. *Nat. Catal.* **2021**, *4* (5), 407−417.
(15) Ding, S.; Lyu, Z.; Fang, L.; Li, T.; Zhu, W.; Li, S.; Li, X.; Li, J.-C.; Du, D.; Lin, Y. Single-Atomic Site Catalyst with Heme Enzymes-Like Active Sites for Electrochemical Sensing of Hydrogen Peroxide. *Small* **2021**, *17* (25), 2100664.
(16) Zhang, R.; Xue, B.; Tao, Y.; Zhao, H.; Zhang, Z.; Wang, X.; Zhou, X.; Jiang, B.; Yang, Z.; Yan, X.; Fan, K. Edge-Site Engineering of Defective Fe-N_4 Nanozymes with Boosted Catalase-Like Performance for Retinal Vasculopathies. *Adv. Mater.* **2022**, *34* (39), 2205324.
(17) Chen, Y.; Jiao, L.; Yan, H.; Xu, W.; Wu, Y.; Zheng, L.; Gu, W.; Zhu, C. Fe-N-C Single-Atom Catalyst Coupling with Pt Clusters Boosts Peroxidase-like Activity for Cascade-Amplified Colorimetric Immunoassay. *Anal. Chem.* **2021**, *93* (36), 12353−12359.
(18) Lyu, Z.; Ding, S.; Zhang, N.; Zhou, Y.; Cheng, N.; Wang, M.; Xu, M.; Feng, Z.; Niu, X.; Cheng, Y.; Zhang, C.; Du, D.; Lin, Y. Single-Atom Nanozymes Linked Immunosorbent Assay for Sensitive Detection of A β 1−40: A Biomarker of Alzheimer's Disease. *Research* **2020**, *2020*, 4724505.
(19) Ge, X.; Liu, Z.; Zhang, W.; Guo, S. Single-Atom Nanocatalysts for Biosensing Application. *CAC* **2022**, *18* (6), 753−763.
(20) Jing, W.; Cui, X.; Kong, F.; Wei, W.; Li, Y.; Fan, L.; Li, X. Fe-N/C Single-Atom Nanozyme-Based Colorimetric Sensor Array for Discriminating Multiple Biological Antioxidants. *Analyst* **2021**, *146* (1), 207−212.
(21) Wang, X.; Gao, X. J.; Qin, L.; Wang, C.; Song, L.; Zhou, Y.-N.; Zhu, G.; Cao, W.; Lin, S.; Zhou, L.; Wang, K.; Zhang, H.; Jin, Z.; Wang, P.; Gao, X.; Wei, H. Eg Occupancy as an Effective Descriptor for the Catalytic Activity of Perovskite Oxide-Based Peroxidase Mimics. *Nat. Commun.* **2019**, *10* (1), 704.
(22) Shen, X.; Wang, Z.; Gao, X.; Zhao, Y. Density Functional Theory-Based Method to Predict the Activities of Nanomaterials as Peroxidase Mimics. *ACS Catal.* **2020**, *10* (21), 12657−12665.
(23) Wang, D.; Song, X.; Li, P.; Gao, X. J.; Gao, X. Origins of the Peroxidase Mimicking Activities of Graphene Oxide from First Principles. *J. Mater. Chem. B* **2020**, *8* (39), 9028−9034.
(24) Gao, X. J.; Yan, J.; Zheng, J.; Zhong, S.; Gao, X. Clear-Box Machine Learning for Virtual Screening of 2D Nanozymes to Target Tumor Hydrogen Peroxide. *Adv. Healthc. Mater.* **2023**, *12* (10), 2202925.
(25) Shen, X.; Wang, Z.; Gao, X. J.; Gao, X. Reaction Mechanisms and Kinetics of Nanozymes: Insights from Theory and Computation. *Adv. Mater.* **2024**, *36*, 2211151.
(26) Xu, B.; Li, S.; Zheng, L.; Liu, Y.; Han, A.; Zhang, J.; Huang, Z.; Xie, H.; Fan, K.; Gao, L.; Liu, H. A Bioinspired Five-Coordinated Single-Atom Iron Nanozyme for Tumor Catalytic Therapy. *Adv. Mater.* **2022**, *34* (15), 2107088.
(27) Pedersen, A.; Barrio, J.; Li, A.; Jervis, R.; Brett, D. J. L.; Titirici, M. M.; Stephens, I. E. L. Dual-Metal Atom Electrocatalysts: Theory, Synthesis, Characterization, and Applications. *Adv. Energy Mater.* **2022**, *12* (3), 2102715.
(28) Xu, J.; Elangovan, A.; Li, J.; Liu, B. Graphene-Based Dual-Metal Sites for Oxygen Reduction Reaction: A Theoretical Study. *J. Phys. Chem. C* **2021**, *125* (4), 2334−2344.
(29) Zhang, S.; Li, Y.; Sun, S.; Liu, L.; Mu, X.; Liu, S.; Jiao, M.; Chen, X.; Chen, K.; Ma, H.; Li, T.; Liu, X.; Wang, H.; Zhang, J.; Yang, J.; Zhang, X.-D. Single-Atom Nanozymes Catalytically Surpassing Naturally Occurring Enzymes as Sustained Stitching for Brain Trauma. *Nat. Commun.* **2022**, *13* (1), 4744.
(30) Du, C.; Gao, Y.; Chen, H.; Li, P.; Zhu, S.; Wang, J.; He, Q.; Chen, W. A Cu and Fe Dual-Atom Nanozyme Mimicking Cytochrome c Oxidase to Boost the Oxygen Reduction Reaction. *J. Mater. Chem. A* **2020**, *8* (33), 16994−17001.
(31) Liu, L.; Zhang, S.; Li, G.; Zhe, Y.; Liu, J.; Zhang, X.; Wei, J.; Sun, X.; Li, Y.; Zhang, X.-D. D-Band Center Coordination Modulated Enzyme-like Activity in Fe-Cu Dual-Metal Single-Atom Nanozymes. *Nano Res.* **2024**, *17*, 5872.
(32) Zeng, R.; Li, Y.; Hu, X.; Wang, W.; Li, Y.; Gong, H.; Xu, J.; Huang, L.; Lu, L.; Zhang, Y.; Tang, D.; Song, J. Atomically Site Synergistic Effects of Dual-Atom Nanozyme Enhances Peroxidase-like Properties. *Nano Lett.* **2023**, *23* (13), 6073−6080.
(33) Liu, Y.; Roy, S.; Sarkar, S.; Xu, J.; Zhao, Y.; Zhang, J. A Review of Carbon Dots and Their Composite Materials for Electrochemical Energy Technologies. *Carbon Energy* **2021**, *3* (5), 795−826.
(34) Fajrial, A. K.; Abdulkarim, M. F.; Saputro, A. G.; Agusta, M. K.; Nugraha; Dipojono, H. K. Boron and Nitrogen Co-Doping Configuration on Pyrolyzed Fe-N_4/C Catalyst. *Procedia Engineering* **2017**, *170*, 131−135.
(35) Wang, Y.; Lai, Y.; Song, L.; Zhou, Z.; Liu, J.; Wang, Q.; Yang, X.; Chen, C.; Shi, W.; Zheng, Y.; Rauf, M.; Sun, S. S-Doping of an Fe/N/C ORR Catalyst for Polymer Electrolyte Membrane Fuel Cells with High Power Density. *Angew. Chem., Int. Ed.* **2015**, *127* (34), 10045−10048.
(36) Li, G.; Liu, H.; Hu, T.; Pu, F.; Ren, J.; Qu, X. Dimensionality Engineering of Single-Atom Nanozyme for Efficient Peroxidase-Mimicking. *J. Am. Chem. Soc.* **2023**, *145* (30), 16835−16842.
(37) Chen, Y.; Jiang, B.; Hao, H.; Li, H.; Qiu, C.; Liang, X.; Qu, Q.; Zhang, Z.; Gao, R.; Duan, D.; Ji, S.; Wang, D.; Liang, M. Atomic-Level Regulation of Cobalt Single-Atom Nanozymes: Engineering High-Efficiency Catalase Mimics. *Angew. Chem., Int. Ed.* **2023**, *62* (19), No. e202301879.

https://doi.org/10.1021/acsomega.4c04990
ACS Omega 2024, 9, 35144−35153

(38) Ding, S.; Barr, J. A.; Lyu, Z.; Zhang, F.; Wang, M.; Tieu, P.; Li, X.; Engelhard, M. H.; Feng, Z.; Beckman, S. P.; Pan, X.; Li, J.; Du, D.; Lin, Y. Effect of Phosphorus Modulation in Iron Single-Atom Catalysts for Peroxidase Mimicking. *Adv. Mater.* **2024**, *36* (10), 2209633.
(39) Jiao, L.; Kang, Y.; Chen, Y.; Wu, N.; Wu, Y.; Xu, W.; Wei, X.; Wang, H.; Gu, W.; Zheng, L.; Song, W.; Zhu, C. Unsymmetrically Coordinated Single Fe-N_3S_1 Sites Mimic the Function of Peroxidase. *Nano Today* **2021**, *40*, 101261.
(40) Liu, W.; Chen, Q.; Wu, J.; Zhang, F.; Han, L.; Liu, J.; Zhang, H.; Hao, Z.; Shi, E.; Sun, Y.; Zhang, R.; Wang, Y.; Zhang, L. Asymmetric Coordination of Iron Single-Atom Nanozymes with Efficient Self-Cascade Catalysis for Ferroptosis Therapy. *Adv. Funct. Mater.* **2024**, *34* (14), 2312308.
(41) Liang, J.; Johannessen, B.; Wu, Z.; Webster, R. F.; Yong, J.; Zulkifli, M. Y. B.; Harbort, J. S.; Cheok, Y. R.; Wen, H.; Ao, Z.; Kong, B.; Chang, S. L. Y.; Scott, J.; Liang, K. Regulating the Coordination Environment of Mesopore-Confined Single Atoms from Metalloprotein-MOFs for Highly Efficient Biocatalysis. *Adv. Mater.* **2022**, *34* (44), 2205674.
(42) Huang, L.; Chen, J.; Gan, L.; Wang, J.; Dong, S. Single-Atom Nanozymes. *Sci. Adv.* **2019**, *5* (5), No. eaav5490.
(43) Wang, Y.; Feng, Q.; Liu, M.; Xue, L.; Wang, G.; Zhang, S.; Hu, W. N, P, S Codoped Carbon Nanozymes with Enhanced Peroxidase-like Activity and Binding Affinity for Total Antioxidant Capacity Assay. *ACS Appl. Nano Mater.* **2023**, *6* (24), 23303−23312.
(44) Li, P.; Guo, Q.; Zhang, J.; Chen, R.; Ding, S.; Su, Y. How the Microenvironment Dominated by the Distance Effect to Regulate the FeN_4 Site ORR Activity and Selectivity? *Nano Res.* **2024**, *17*, 5735.
(45) Hu, Y.; Gao, X. J.; Zhu, Y.; Muhammad, F.; Tan, S.; Cao, W.; Lin, S.; Jin, Z.; Gao, X.; Wei, H. Nitrogen-Doped Carbon Nanomaterials as Highly Active and Specific Peroxidase Mimics. *Chem. Mater.* **2018**, *30* (18), 6431−6439.
(46) Li, K.; Zhang, S.; Zhang, X.; Liu, S.; Jiang, H.; Jiang, T.; Shen, C.; Yu, Y.; Chen, W. Atomic Tuning of Single-Atom Fe-N-C Catalysts with Phosphorus for Robust Electrochemical CO_2 Reduction. *Nano Lett.* **2022**, *22* (4), 1557−1565.
(47) Niu, J.; Qi, W.; Li, C.; Mao, M.; Zhang, Z.; Chen, Y.; Li, W.; Ge, S. Mechanisms of Oxygen Reduction Reaction on B Doped FeN_4-G and FeN_4-CNT Catalysts for Proton-Exchange Membrane Fuel Cells. *Int. J. Energy Res.* **2021**, *45* (6), 8524−8535.
(48) Lin, Y.; Liu, K.; Chen, K.; Xu, Y.; Li, H.; Hu, J.; Lu, Y.-R.; Chan, T.-S.; Qiu, X.; Fu, J.; Liu, M. Tuning Charge Distribution of FeN_4 via External N for Enhanced Oxygen Reduction Reaction. *ACS Catal.* **2021**, *11* (10), 6304−6315.
(49) Yin, H.; Yuan, P.; Lu, B.-A.; Xia, H.; Guo, K.; Yang, G.; Qu, G.; Xue, D.; Hu, Y.; Cheng, J.; Mu, S.; Zhang, J.-N. Phosphorus-Driven Electron Delocalization on Edge-Type FeN_4 Active Sites for Oxygen Reduction in Acid Medium. *ACS Catal.* **2021**, *11* (20), 12754−12762.
(50) Jia, Y.; Xiong, X.; Wang, D.; Duan, X.; Sun, K.; Li, Y.; Zheng, L.; Lin, W.; Dong, M.; Zhang, G.; Liu, W.; Sun, X. Atomically Dispersed Fe-N_4 Modified with Precisely Located S for Highly Efficient Oxygen Reduction. *Nano-Micro Lett.* **2020**, *12* (1), 116.
(51) Kresse, G.; Furthmüller, J. Efficiency of Ab-Initio Total Energy Calculations for Metals and Semiconductors Using a Plane-Wave Basis Set. *Comput. Mater. Sci.* **1996**, *6* (1), 15−50.
(52) Kresse, G.; Furthmüller, J. Efficient Iterative Schemes for *Ab Initio* Total-Energy Calculations Using a Plane-Wave Basis Set. *Phys. Rev. B* **1996**, *54* (16), 11169−11186.
(53) Blöchl, P. E. Projector Augmented-Wave Method. *Phys. Rev. B* **1994**, *50* (24), 17953−17979.
(54) Kresse, G.; Joubert, D. From Ultrasoft Pseudopotentials to the Projector Augmented-Wave Method. *Phys. Rev. B* **1999**, *59* (3), 1758−1775.
(55) Perdew, J. P.; Burke, K.; Ernzerhof, M. Generalized Gradient Approximation Made Simple. *Phys. Rev. Lett.* **1996**, *77* (18), 3865−3868.
(56) Grimme, S.; Antony, J.; Ehrlich, S.; Krieg, H. A Consistent and Accurate *Ab Initio* Parametrization of Density Functional Dispersion Correction (DFT-D) for the 94 Elements H-Pu. *J. Chem. Phys.* **2010**, *132* (15), 154104.
(57) Grimme, S.; Ehrlich, S.; Goerigk, L. Effect of the Damping Function in Dispersion Corrected Density Functional Theory. *J. Comput. Chem.* **2011**, *32* (7), 1456−1465.
(58) Monkhorst, H. J.; Pack, J. D. Special Points for Brillouin-Zone Integrations. *Phys. Rev. B* **1976**, *13* (12), 5188−5192.
(59) Anisimov, V. I.; Zaanen, J.; Andersen, O. K. Band Theory and Mott Insulators: Hubbard *U* Instead of Stoner *I*. *Phys. Rev. B* **1991**, *44* (3), 943−954.
(60) Deringer, V. L.; Tchougréeff, A. L.; Dronskowski, R. Crystal Orbital Hamilton Population (COHP) Analysis As Projected from Plane-Wave Basis Sets. *J. Phys. Chem. A* **2011**, *115* (21), 5461−5466.
(61) Maintz, S.; Deringer, V. L.; Tchougréeff, A. L.; Dronskowski, R. LOBSTER: A Tool to Extract Chemical Bonding from Plane-Wave Based DFT: Tool to Extract Chemical Bonding. *J. Comput. Chem.* **2016**, *37* (11), 1030−1035.
(62) Koningsberger, D. C.; Prins, R. *X-ray Absorption: Principles, Applications, Techniques of EXAFS, SEXAFS and XANES*; Wiley, 1988.
(63) Jia, Y.; Zhang, L.; Zhuang, L.; Liu, H.; Yan, X.; Wang, X.; Liu, J.; Wang, J.; Zheng, Y.; Xiao, Z.; Taran, E.; Chen, J.; Yang, D.; Zhu, Z.; Wang, S.; Dai, L.; Yao, X. Identification of Active Sites for Acidic Oxygen Reduction on Carbon Catalysts with and without Nitrogen Doping. *Nat. Catal.* **2019**, *2* (8), 688−695.
(64) Wang, X.; Fu, Y.; Tranca, D.; Jiang, K.; Zhu, J.; Zhang, J.; Han, S.; Ke, C.; Lu, C.; Zhuang, X. Regulating the Spin State of Nickel in Molecular Catalysts for Boosting Carbon Dioxide Reduction. *ACS Appl. Energy Mater.* **2021**, *4* (3), 2891−2898.
(65) He, J.; Zheng, T.; Wu, D.; Zhang, S.; Gu, M.; He, Q. Insights into the Determining Effect of Carbon Support Properties on Anchoring Active Sites in Fe-N-C Catalysts toward the Oxygen Reduction Reaction. *ACS Catal.* **2022**, *12* (3), 1601−1613.
(66) Pan, L.; Ai, M.; Huang, C.; Yin, L.; Liu, X.; Zhang, R.; Wang, S.; Jiang, Z.; Zhang, X.; Zou, J.-J.; Mi, W. Manipulating Spin Polarization of Titanium Dioxide for Efficient Photocatalysis. *Nat. Commun.* **2020**, *11* (1), 418.
(67) Zhou, X.; Gao, J.; Hu, Y.; Jin, Z.; Hu, K.; Reddy, K. M.; Yuan, Q.; Lin, X.; Qiu, H.-J. Theoretically Revealed and Experimentally Demonstrated Synergistic Electronic Interaction of CoFe Dual-Metal Sites on N-Doped Carbon for Boosting Both Oxygen Reduction and Evolution Reactions. *Nano Lett.* **2022**, *22* (8), 3392−3399.
(68) Wang, Y.; Cho, A.; Jia, G.; Cui, X.; Shin, J.; Nam, I.; Noh, K.; Park, B. J.; Huang, R.; Han, J. W. Tuning Local Coordination Environments of Manganese Single-Atom Nanozymes with Multi-Enzyme Properties for Selective Colorimetric Biosensing. *Angew. Chem., Int. Ed.* **2023**, *135* (15), No. e202300119.

https://doi.org/10.1021/acsomega.4c04990
ACS Omega 2024, 9, 35144−35153